Energy 172 (2019) 661–674

Contents lists available at ScienceDirect

Energy

journal homepage: www.elsevier.com/locate/energy

A comprehensive understanding of enhanced condensation heat transfer using phase separation concept

Jian Xie [a], Jinliang Xu [a, *], Cong Liang [a], Qingting She [a], Mingjia Li [b]

[a] The Beijing Key Laboratory of Multiphase Flow and Heat Transfer, North China Electric Power University, Beijing 102206, China
[b] Key Laboratory of Thermo-Fluid Science and Engineering of Ministry of Education, School of Energy & Power Engineering, Xi'an Jiaotong University, Xi'an, Shaanxi 710049, China

ARTICLE INFO

Article history:
Received 23 October 2018
Received in revised form
14 January 2019
Accepted 26 January 2019
Available online 31 January 2019

Keywords:
Condensation heat transfer
Mesh screen
Flow pattern
Droplet dynamics
Wettability

ABSTRACT

A comprehensive analysis of enhanced condensation with phase separation concept is presented, for which mesh-membrane-tube (MMT) is suspended in a tube. A twill Dutch weaved mesh screen and two plain Dutch weaved mesh screens are used to fabricate MMT. Our study reveals that liquid leakage across MMT not only keeps better condensation on condenser wall, but also decreases pressure drop rise penalty. To modulate stratified-flow, the #1 MMT with smallest d_p has the largest capillary force to pump liquid towards core region to expose more condenser surface with vapor, where d_p is pore diameter. To modulate annular-flow, finest mesh wires of #1 MMT ensure the best wetting to liquid to prevent condenser wall from being impacted by satellite droplets. These mechanisms explain the best performance of #1 MMT, reaching a maximum heat transfer enhancement ratio of 1.82. The three MMTs share a single curve of nozzle discharge coefficient versus Reynolds number. The similar performance of #2 and #3 MMTs is due to identical d_p/φ, where φ is mesh open porosity. Fine mesh wires and small mesh pores are suggested to enhance condensation heat transfer. MMT are recommended to be used in condenser tube upstream when vapor mass qualities larger than 0.1.

1. Introduction

There are various low-grade thermal energies such as solar energy, geothermal energy and waste heat [1–3]. Organic fluids, due to their low boiling points, are attractive to recover low-grade energy to generate power using organic Rankine cycle (ORC) [4]. In such a system, condensation heat transfer coefficients are even lower than convective heat transfer coefficients of water, inducing huge heat transfer area [5]. For example, an ocean thermal energy conversion plant should have a heat transfer area ~10^4 m^2/MW [6]. Condensation heat transfer should be enhanced to reduce the cost for low-grade energy utilization [7].

The condenser tubes with extended heat transfer surfaces or twisted tape inserts are widely used for heat transfer enhancement. In refrigeration system, condenser tubes have a ~8 mm diameter, limiting the utilization of insert. Corrugated tube [8], micro-fin tube [9] and grooved tube [10] belong to the extended surface tubes, which are suitable for small sized tubes. Wang et al. [11] fabricated 3D structure such as circumferential or twisted pin fins by selective laser melting to extend wall surface area to enhance condensation heat transfer in tube. Udaya Kumar et al. [12] modified the wettability of the grooved wall surface by the dip coating technique to enhance condensation heat transfer. For applications such as a 50 kW ORC system, condenser tubes have larger diameter such as 19 mm [13], making it possible to use tube inserts. Refs. [14–16] reported the in-tube heat transfer enhancement with twisted tape inserts, caused by boundary layer destruction and secondary flow generation.

Nusselt [17] pointed out that the condensation heat transfer coefficient is determined by liquid film thickness on tube wall. For convective condensation in tubes, Breber et al. [18], Shah [19] and Dobson & Chato [20] noted that the liquid film thickness is influenced by two-phase flow patterns. Recently, the phase separation concept was introduced to enhance the condensation heat transfer in tubes [21–23]. The mesh-membrane-tubes (MMT) are suspended in a tube, separating the tube cross-section into a core region inside MMT and an annular region between tube wall and MMT. When a two-phase mixture interacts MMT, liquid flows towards core region due to capillary effect induced by mesh-pores,

* Corresponding author.
E-mail address: xjl@ncepu.edu.cn (J. Xu).

https://doi.org/10.1016/j.energy.2019.01.134
0360-5442/

Nomenclature

A_s	wetting area, m^2
b	attenuation coefficient, s^{-1}
B	constant parameter in Eq. (37)
Bn	Bond number
C	constant parameter in Eq. (17)
C_d	nozzle discharge coefficient
C_p	specific heat of cooling water, kJ/(kg K)
C_∞	constant parameter in Eq. (37)
d_o	diameter of MMT insert, m
d_p	mesh pore diameter, m
D_{gl}	inner diameter of sight glass tube, m
D_i	inner diameter of copper tube, m
D_{ins}	inner diameter of stainless-steel tube, m
D_o	outer diameter of copper tube, m
e_A	average absolute deviation
e_R	average deviation
EF	heat transfer enhancement ratio
Fr	Froude number
F_σ	capillary force, N
g	gravity acceleration, m/s^2
G	mass flux, $kg/(m^2s)$
G_{leak}	superficial mass flux across MMT, $kg/(m^2s)$
h	condensation heat transfer coefficient, $W/(m^2K)$
h_c	heat transfer coefficient of cooling water, $W/(m^2K)$
h_{total}	total heat transfer coefficient, $W/(m^2K)$
H_l	liquid height in tube bottom, m
i	enthalpy, J/kg
i_l	saturation enthalpy of liquid, J/kg
i_v	saturation enthalpy of vapor, J/kg
I	current, A
k	thermal conductivity of copper tube, W/(m K)
K	nozzle pressure drop coefficient
K_1	non-dimensional parameter defined in Eq. (25)
K_2	non-dimensional parameter defined in Eq. (28)
L	length of sight glass tube, m
L_{eff}	effective length of heat exchange, m
L_m	length of MMT, m
$LMTD$	logarithm mean temperature difference, °C
m	mass flow rate, kg/s
n	constant parameter in Eq. (37)
P	organic fluid pressure, Pa
P_{crit}	critical pressure of R245fa, Pa
P_{sat}	saturation pressure, Pa
ΔP	total pressure drop, Pa
ΔP_a	acceleration pressure drop, Pa
ΔP_f	frictional pressure drop, Pa
ΔP_σ	capillary pressure difference, Pa
PEC	performance evaluation parameter
PF	pressure drop penalty ratio
Pr	Prandtl number
Q	heat transfer rate of test section, W
Re_p	Reynolds number
S_v	area exposed in vapor per unit length, m
t	time, s
T	temperature, °C
ΔT	temperature difference, °C
U	voltage, V
We	Weber number
x	vapor mass quality
$\tilde{x}_1, \tilde{x}_2, \ldots \tilde{x}_n$	independent variables
$\Delta\tilde{x}_1, \Delta\tilde{x}_2, \ldots \Delta\tilde{x}_n$	uncertainties of independent parameters
X	Martinetti number
Y	any dependent variable
z	distance along R245fa flow direction, m

Greek symbols

α	void fraction
θ	contact angle
δ	mesh wire diameter, m
λ	thermal conductivity, W/(m K)
μ	dynamic viscosity, Pa s
ρ	density, kg/m^3
σ	surface tension force, N/m
σ_n	standard deviation
ϕ_l^2	two-phase flow frictional factor
φ	mesh open porosity
ω	curvature of liquid-vapor interface, m
ν	kinematic viscosity, m^2/s

Subscript

1	evaporator inlet
2	evaporator outlet
an	annular region
ave	average value
A	A-A cross section in Fig. 12
b	bottom location
B	B-B cross section in Fig. 12
BT	bare tube
c	cooling water
co	core region
e	exit of MMT
in	test section inlet
j	cross section member
l	liquid
MMT	mesh-membrane-tube
out	test section outlet
pre	prediction value
r	organic fluid
s	side location
t	top location
u	upstream of MMT
v	vapor
w	wall
wa	warp wire
we	weft wire

leaving gas flowing in annular region to create thin liquid film on tube wall. The condenser tube has been authorized by a U.S. patent [21]. Both our experimental and numerical work with adiabatic air-water two-phase flow confirm the phase separation to create thin liquid film on the wall [22,23].

Fundamentally, the method to complete the phase separation is to use the surface energy principle. Considering a two-phase mixture in a larger space contacted with a micro-structure, if a bubble is enforced to penetrate the micro-structure, the surface energy of the bubble should be increased. Thus, the vapor phase is kept in the larger space but the liquid can flow across the micro-structure. Practically, the micro-structure can be the mesh screen porous such as studied in this paper. Alternatively, the micro-structure can also be the particle sintered wick [24].

By inserting a powder-sintering-membrane in a tube, condensation heat transfer coefficients are 1.85 times of bare tube [24]. By suspending a mesh-screen-membrane in a tube, heat transfer coefficients are two times of bare tube [25]. It is observed that the phase separation concept is not only useful for large size condenser [26], but also effective in microchannel condensers [27]. Yu et al. [27] proposed a phase separation micro-condenser to obviously raise the condensation heat transfer coefficients. It is surprising to find the decreased pressure drops, as long as the vapor tunnel is not flooded by liquid.

Our previous work focused on using porous material with specific structure parameters to enhance condensation heat transfer [24,25]. The objective of this paper is to (1) identify key porous-structure-parameters which are important to influence condenser performance, (2) analyze the mechanisms regarding effects of these parameters on condensation heat transfer, and (3) recommend future research and development. The paper structure is organized as follows. Section 2 deals with experiment setup, test section, data reduction and calibration. Section 3 deals with results and discussion, including section 3.1 for heat transfer performance, section 3.2 for flow pattern measurement, section 3.3 for annular-flow-pattern modulation, section 3.4 for stratified-flow-pattern modulation. Section 4 explains why we need to use the porous membrane tube for condensation. The new findings are summarized in section 5.

2. Experimental setup

2.1. Experimental loop

The experimental setup consisted of an organic fluid loop and a chiller water loop (see Fig. 1). The organic fluid loop was vacuumed to remove non-condensable gas, followed by charging R245fa liquid. R245fa was pumped by a diaphragm pump to be circulating in the loop. The mass flow rate of R245fa, m_r, was controlled by setting a diaphragm displacement and measured by a mass flow meter. At the diaphragm pump outlet, an accumulator stabilized the fluid pressure.

To generate vapor-liquid mixture, the R245fa liquid was evaporated in an evaporator, which was a helically coiled tube directly heated by an alternative current (AC). For such heating, a transformer converted a high AC voltage 380 V to a low voltage U. The evaporator was electrically insulated from other components. The evaporator inlet was subcooled liquid having a temperature $T_{r,1}$. The evaporator outlet was the two-phase mixture having a saturation temperature $T_{r,2}$. The vapor mass quantity at the evaporator outlet can be changed by adjusting voltage U.

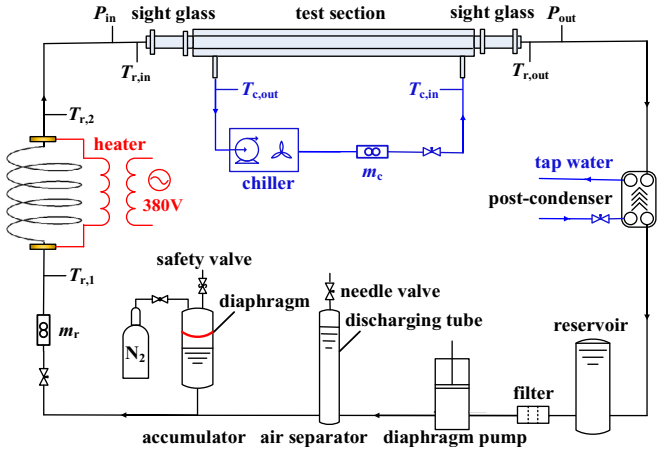

Fig. 1. The experimental setup.

The two-phase mixture was condensed in a condenser tube test section by circulating chiller water in tube annulus. The cooling water was provided by a chiller, with the mass flow m_c measured by a mass flow meter. Two jacket-thermocouples measured the inlet and outlet temperatures of the chiller water, $T_{c,in}$ and $T_{c,out}$, respectively. In the organic fluid side, the fluid temperatures/pressures at the test section inlet and outlet ($T_{r,in}$, $T_{r,out}$, P_{in} and P_{out}) were measured by jacket-thermocouples and pressure transducers. The mixture at the condenser outlet was further condensed to subcooled liquid in a post-condenser, then returned to a liquid tank reservoir.

2.2. Test section

The test section is a counter-current condenser tube, consisting of a copper tube and a shell stainless-steel tube (see Fig. 2). The R245fa mixture flowed in the copper tube with an inner diameter $D_i = 14.73$ mm and an outer diameter $D_o = 19.02$ mm. The stainless-steel tube had an inner diameter $D_{ins} = 23.35$ mm. Cooling water was flowing in the tube annulus between copper tube and shell tube. In order to observe flow patterns of R245fa mixture, two sight-glass tubes were connected with the copper tube by flanges at the test section inlet and outlet. A high-speed camera (Motion pro Y4, IDT) recorded flow pattern images with a frequency of 4000 fps. The visualization size was 80×80 mm, corresponding to 1016×1016 pixels to have a size resolution of 79 μm. Table 1 shows the structure parameters of the test section.

Six cross-sections 1–6 were arranged along flow direction, having a neighboring distance of 200 mm (see Fig. 2a). On each cross-section, three thermocouples measured wall temperatures $T_{j,w,t}$ $T_{j,w,s}$ and $T_{j,w,b}$, where j means the number of cross-section, w means wall, t, s and b stand for top wall, side wall and bottom wall, respectively. Sheathed thermocouples in tube annulus center measured cooling water temperature $T_{j,c}$. For data reduction, the inlet and outlet cooling water temperatures are averaged by the three thermocouples at cross-sections 1 and 6 (see Fig. 2b). Except the inlet and outlet cross-sections, one cross-section only had one thermocouple to measure the cooling water temperatures (see Fig. 2c).

Condensation of R245fa was performed in bare tube (BT) and

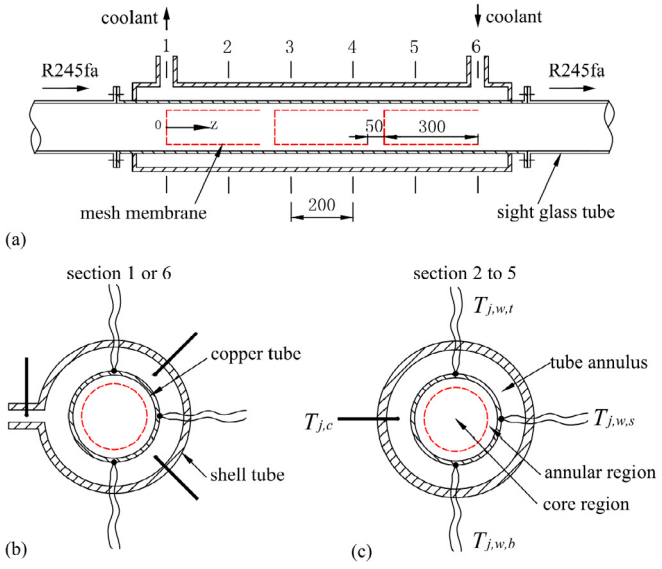

Fig. 2. The test section.

Table 1
The major parameters for condenser tube package.

Components	Materials	Parameters
shell tube	304 stainless steel	$D_{ins} = 23.35$ mm
copper tube	T2 type copper	$D_i = 14.73$ mm, $D_o = 19.02$ mm, $L_{eff} = 1000$ mm
sight glass tube	transparent quartz	$D_{gl} = 15.80$ mm, $L = 200$ mm
mesh membrane tube	316 stainless steel	$d_o = 11.40$ mm, $L_m = 300$ mm
mesh screen #1	316 stainless steel	$d_p = 15$ μm, $\delta_{wa} = 63$ μm, $\delta_{we} = 40$ μm, $\varphi = 11.4\%$
mesh screen #2	316 stainless steel	$d_p = 32$ μm, $\delta_{wa} = 125$ μm, $\delta_{we} = 63$ μm, $\varphi = 13.2\%$
mesh screen #3	316 stainless steel	$d_p = 50$ μm, $\delta_{wa} = 140$ μm, $\delta_{we} = 100$ μm, $\varphi = 20.0\%$

modulated condenser tube with MMT insert. Because short MMT inserts are better than a longer one [28], three short MMT inserts were suspended in the copper tube, each having a length of 300 mm. The gap between two neighboring MMTs was 50 mm (see Fig. 2a). The MMT insert divided the tube cross-section into an annular region and a core region (see Fig. 2c).

It is difficult to arrange thermocouple wires on copper wall. A smart solution is shown in Fig. 3. By hitting copper tube with a point chisel, a thin copper film was being lifted up from copper tube surface to generate a cavity, in which a thermocouple wire was buried. The thermocouple wire was tightly attached on the wall by hitting a blunt chisel on the copper film (see Fig. 3a). Each thermocouple wire was penetrated through a hole on shell tube wall. Finally, all the "extra" thermocouple wires were pulled out of the shell tube simultaneously, until they were "standing" in the gap between copper tube and shell tube (see Fig. 3b). The integration of MMTs with copper tube is shown in Fig. 3c. Short copper wires connected neighboring MMTs by welding. The copper wires on the first MMT were buried in two grooves at the copper tube inlet. As the supporting structure, three copper wires were uniformly distributed over the tube cross-section to ensure uniform gap between copper tube and MMT.

Two types of mesh screen are used to fabricate MMT. The scanning-electron-microscope (SEM) images are provided in Fig. 4a for twill Dutch weaved mesh screen and Fig. 4b and c for plain Dutch weaved mesh screen. Fig. 4d and e show the cross-section

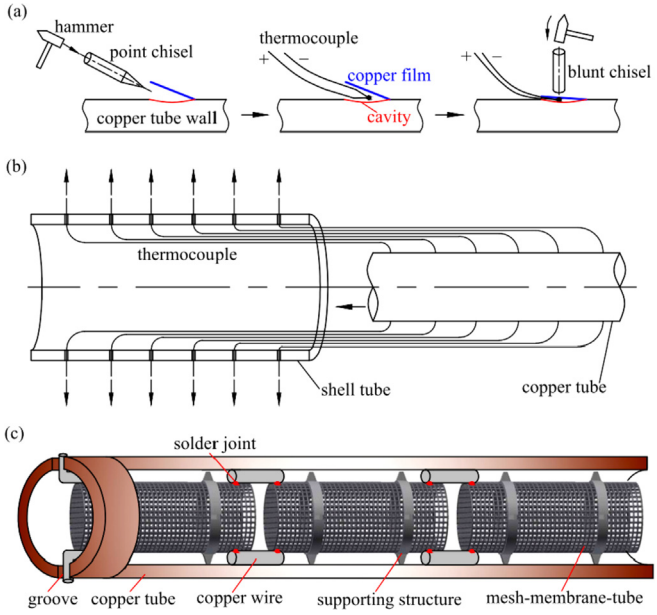

Fig. 3. The integration of condenser tube with MMT insert (a: thermocouple wires buried in cavities on copper tube wall; b: pulling extra thermocouple wires out of the tube annulus between shell tube and copper tube; c: integration of MMT insert in condenser tube).

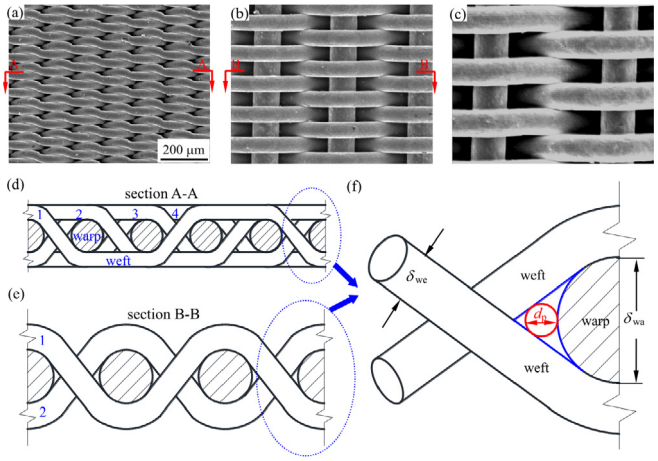

Fig. 4. Images showing mesh screen to fabricate MMT insert (a for #1 twill Dutch weaved mesh screen; b and c for #2 and 3 plain Dutch weaved mesh screen; d for cross-section of #1 mesh screen in depth direction; e for cross-section of #2 mesh screen in depth direction; f for definitions of d_p, δ_{we} and δ_{wa}).

views for the two types of mesh screen. Four parameters characterize the mesh screen: weft wire diameter δ_{we}, warp wire diameter δ_{wa}, superficial pore diameter d_p and open porosity φ, in which d_p means the maximum size of a particle that can successfully fall down through mesh pore, and φ is the ratio of mesh pore area to the project area (see Fig. 4f). Table 1 lists all these parameters.

2.3. Data reduction and uncertainty analysis

Inlet and outlet vapor mass qualities of test section: The vapor mass quality of two-phase mixture at the condenser tube inlet x_{in} is

$$x_{in} = \frac{i_{r,1} + UI/m_r - i_{l,in}}{i_{v,in} - i_{l,in}} \quad (1)$$

where $i_{r,1}$ is the enthalpy at the inlet of the helically coiled tube, $i_{v,in}$ and $i_{l,in}$ are the saturation vapor and liquid enthalpies at the test section inlet, corresponding to the inlet pressure P_{in}. The heat transfer rate of the condenser tube test section Q is

$$Q = m_c C_{p,c}(T_{c,out} - T_{c,in}) \quad (2)$$

where $C_{p,c}$ is the specific heat of cooling water.

The vapor mass quality of two-phase mixture at the test section outlet is

$$x_{out} = \frac{i_{r,1} + UI/m_r - Q/m_r - i_{l,out}}{i_{v,out} - i_{l,out}} \quad (3)$$

where $i_{v,out}$ and $i_{l,out}$ are the enthalpies of saturation R245fa vapor

and liquid based on P_{out}.

Condensation heat transfer coefficient of R245fa: Based on thermal resistance analysis [29], condensation heat transfer coefficient of R245fa in the copper tube is

$$h = \frac{1}{\frac{1}{h_{total}} - \frac{D_i}{2k}\ln\left(\frac{D_o}{D_i}\right) - \frac{D_i}{D_o}\frac{1}{h_c}} \tag{4}$$

where k is the thermal conductivity of copper tube. The total heat transfer coefficient h_{total} is:

$$h_{total} = \frac{Q}{\pi D_i L_{eff} \bullet LMTD} \tag{5}$$

where L_{eff} is the effective length of the condenser tube. The logarithm mean temperature difference $LMTD$ is

$$LMTD = \frac{(T_{r,in} - T_{c,out}) - (T_{r,out} - T_{c,in})}{\ln\left(\frac{T_{r,in} - T_{c,out}}{T_{r,out} - T_{c,in}}\right)} \tag{6}$$

In Eq. (4), h_c is the forced convective heat transfer coefficient of cooling water:

$$h_c = \frac{D_i Q}{\pi D_o L_{eff}(T_{w,ave} - T_{c,ave})} \tag{7}$$

where $T_{w,ave}$ is the averaged wall temperature measured by thermocouple wires.

Pressure drop of R245fa: For two-phase flow in horizontal tube, the total pressure drop ΔP includes frictional component ΔP_f and acceleration component ΔP_a:

$$\Delta P = \Delta P_f + \Delta P_a = P_{in} - P_{out} \tag{8}$$

ΔP_a is

$$\Delta P_a = G^2\left[\frac{x^2}{\rho_v \alpha} + \frac{(1-x)^2}{\rho_l(1-\alpha)}\right]_{out} - G^2\left[\frac{x^2}{\rho_v \alpha} + \frac{(1-x)^2}{\rho_l(1-\alpha)}\right]_{in} \tag{9}$$

where ρ_l and ρ_v are the liquid and vapor densities of R245fa, respectively. The R245fa mass flux is $G = \frac{4m_r}{\pi D_i^2}$, α is the void fraction calculated by the Smith formula [30]:

$$\alpha = \left\{1 + \frac{\rho_v}{\rho_l}\left(\frac{1-x}{x}\right)\left[0.4 + 0.6\left(\frac{\frac{\rho_l}{\rho_v} + 0.4\frac{1-x}{x}}{1 + 0.4\frac{1-x}{x}}\right)^{1/2}\right]\right\}^{-1} \tag{10}$$

The frictional pressure drop ΔP_f is the total pressure drop subtracting the accelerating component.

Evaluation of the condenser tube performance: The heat transfer enhancement ratio EF is

$$EF = \frac{h_{MMT}}{h_{BT}} \tag{11}$$

where h_{MMT} and h_{BT} are the condensation heat transfer coefficients for tubes with MMT insert and without MMT insert (BT), respectively.

The pressure drop penalty ratio PF is

$$PF = \frac{\Delta P_{f,MMT}}{\Delta P_{f,BT}} \tag{12}$$

The performance evaluation parameter PEC considers both the heat transfer enhancement and the pressure drop penalty [31,32].

$$PEC = \frac{EF}{PF^{1/6}} \tag{13}$$

Uncertainty analysis: High accuracy sensors measured various parameters. For operation, the controlling parameters are the R245fa liquid temperature at evaporator inlet ($T_{r,1}$), inlet cooling water temperature ($T_{c,in}$) and inlet pressure P_{in}, which are 10 ± 0.4 °C, 25 ± 0.3 °C and 250 ± 5 kPa, respectively. For practical applications, the economic flow velocity of liquid is ~1 m/s. Two-phase flow has larger pressure drop than single-phase liquid flow. The mass flux for a condensing flow should be smaller than 1000 kg/m^{2}s [33]. Thus, the present paper covered the range of mass fluxes of 198.8–709.4 kg/(m^{2}s). Table 2 shows the ranges for all the measured parameters. Mass flow rates were measured by DMF-1-DX mass flow meters with an uncertainty of 0.1%. Temperatures were measured by Omega K-type thermocouples with an uncertainty of 0.2 °C. Pressures were measured by Rosemount-3051 pressure transducers with an uncertainty of 1.0%. Both voltage and current applied to evaporator had the uncertainties of 1.0%. The parameters h, EF and PEC were calculated based on measured parameters, whose uncertainties were evaluated by the error transmission theory [34]. If Y is a given function of the independent variables of $\tilde{x}_1$, $\tilde{x}_2$ … $\tilde{x}_n$ and $\Delta\tilde{x}_1$, $\Delta\tilde{x}_2$ … $\Delta\tilde{x}_n$ are the uncertainties of these independent parameters, the uncertainty of Y is

$$\Delta Y = \sqrt{\left(\frac{\partial Y}{\partial \tilde{x}_1}\Delta\tilde{x}_1\right)^2 + \left(\frac{\partial Y}{\partial \tilde{x}_2}\Delta\tilde{x}_2\right)^2 + \ldots\ldots\left(\frac{\partial Y}{\partial \tilde{x}_n}\Delta\tilde{x}_n\right)^2} \tag{14}$$

According to Eq. (14), the uncertainties of h, EF and PEC were 10.18%, 13.78% and 13.83%, respectively (see Table 3).

Calibration experiment for bare tube BT: Because the content of non-condensable gas obviously affects the partial vapor pressure, the relationship between vapor pressure and temperature was examined. We show that the measured vapor pressure and temperature matched the relationship assuming no non-condensable gas at saturation state. For example, having a run with $G = 198.04$ kg/m^{2}s and $x_{in} = 0.401$, the saturation temperature was 55.4 °C at $P_{in} = 408.4$ kPa based on REFPROP, and the measured temperature was 55.3 °C, showing only 0.1 °C deviation between the two temperatures.

Condensation heat transfer coefficients and pressure drops in bare tube are calibrated. The former can be predicted by the Shah correlation [19]:

$$h_{BT,pre} = 0.023\frac{\lambda_l}{D_i}\left(\frac{GD_i}{\mu_l}\right)^{0.8} Pr_l^{0.4}\left[1 + 3.8\left(\frac{x_{BT}}{1 - x_{BT}}\sqrt{\frac{P_{crit}}{P_{sat}}}\right)^{0.76}\right] \tag{15}$$

where λ_l, μ_l and Pr_l are the thermal conductivity, dynamic viscosity and Prandtl number of R245fa liquid at saturation pressure P_{sat},

Table 2
The data ranges of major measured parameters.

Parameters	Ranges
mass flux of R245fa flow (kg/m^{2}s)	198.8–709.4
inlet temperature of the helical-coiled tube (°C)	15.0 ± 0.3
inlet pressure of the test section (kPa)	405.0 ± 4.0
inlet temperature of the test section (°C)	55.5 ± 0.3
inlet vapor mass quality of the test section	0.032–0.940
mass flow rates of the cooling water (kg/h)	500.0 ± 4.0
inlet temperature of the cooling water (°C)	20.0 ± 0.3
heat flux on the inner wall surface (kW/m^2)	21.38–105.95

Table 3
The major parameters, instruments and uncertainties.

Parameters	Instruments	Uncertainties
wall temperature	K-type thermocouple wire	0.2 °C
fluid temperature	K-type jacket thermocouple	0.2 °C
R245fa mass flow rate	DMF-1-DX mass flow meter	0.1%
cooling water mass flow rate	DMF-1-DX mass flow meter	0.1%
Pressure	Rosemount-3051 pressure transducer	1.0%
h		2.10–10.18%
EF		3.31–13.78%
PEC		3.45–13.83%

which is the mean value of P_{in} and P_{out}. x_{BT} is the average vapor mass quality based on x_{in} and x_{out}, P_{crit} is the critical pressure of R245fa.

The three deviations e_R, e_A and σ_n characterize the matching degree between measured and predicted values [35]. Fig. 5a shows that the three values are −4.45%, 5.10% and 5.19%, respectively, illustrating perfect agreement for two-phase heat transfer. The Chisholm model [36] predicts the friction pressure drop in bare tube as

$$\Delta P_{f,BT} = 0.3164\phi_l^2 \frac{G^{1.5}(1-x_{BT})^{1.75}\mu_l^{0.25}L_{eff}}{D_i^{1.25}\rho_l} \tag{16}$$

$$\phi_l^2 = 1 + \frac{C}{X} + \frac{1}{X^2} \tag{17}$$

where X is the Martinetti number:

$$X = \left(\frac{\rho_v}{\rho_l}\right)^{0.5}\left(\frac{1-x_{BT}}{x_{BT}}\right)^{0.9}\left(\frac{\nu_l}{\nu_v}\right)^{0.1} \tag{18}$$

where ν_l and ν_v are the kinematic viscosities of R245fa liquid and vapor, respectively, the parameter C is based on if the flow is laminar or turbulent. Both phases of vapor and liquid in laminar regime yields $C = 5$. The turbulent flow for both phases yields $C = 20$. In this study, the two phases of liquid and vapor are in laminar regime and turbulent regime respectively. It is reasonable to observe the C ranges between 5 and 20 based on our experimental data (see Fig. 5b).

3. Result and discussion

Here, we present the measured flow and heat transfer data, concluding the #1 MMT insert to have the best performance. The flow pattern observation shows that the annular flow and stratified flow are the major flow patterns. Then, we analyze how the mesh screen parameters influence the modulation of the two major flow patterns, explaining the observed heat transfer data.

3.1. Heat transfer enhancement with MMT insert

Fig. 6 shows wall temperatures for bare tube and three condenser tubes with different MMT inserts. The general trend is the decreased wall temperatures along flow direction, due to the flow from left to right. In each subfigure, three temperature curves represent the top, side and bottom locations (see Fig. 2c). For two-phase horizonal flow, the vapor phase has the trend to populate on the top location. The top locations (red curves) have slightly higher temperatures than other locations. Among the four condenser tubes, wall temperatures are lowest for the bare tube, and highest for the tube with #1 MMT insert to indicate the best performance.

Fig. 7 illustrates thermal-hydraulic performances of the four

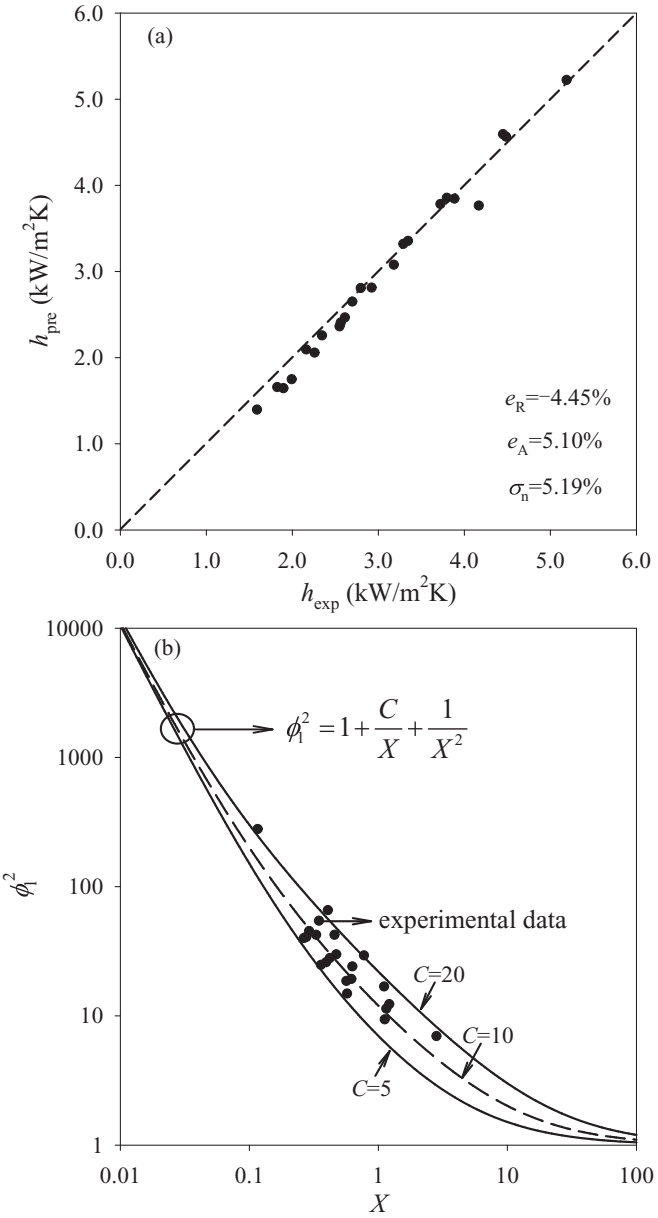

Fig. 5. Comparison of measured condensation heat transfer and pressure drop in bare tube with correlations in the literature (a for heat transfer coefficients in which the predictions are coming from the Shah correlation [19]; b for two-phase multiplier with solid curves calculated by the Chisholm model [36] with C in the reasonable range of 5–10).

condenser tubes. Condensation heat transfer coefficients are increased with increases of mass fluxes G and/or vapor mass qualities x (see Fig. 7a and c). Compared with BT, the three condenser tubes with MMT inserts enhance condensation heat

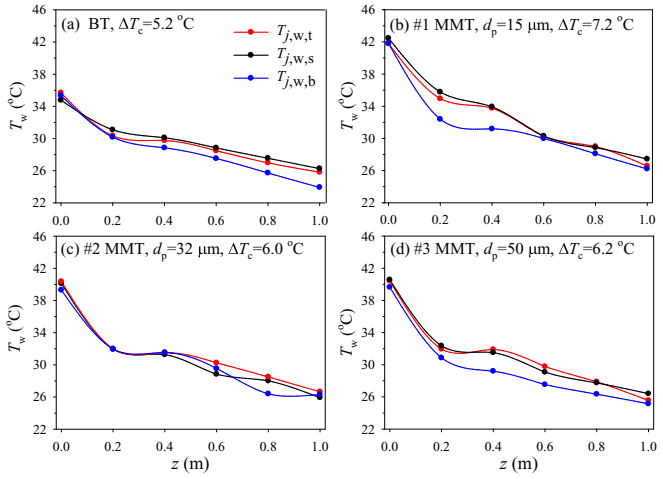

Fig. 6. Wall temperatures along flow direction for bare tube BT and the three condenser tubes with different MMT inserts having similar conditions of $G = 198.5 \pm 0.5$ kg/m^{2}s and $x_{in} = 0.908 \pm 0.004$.

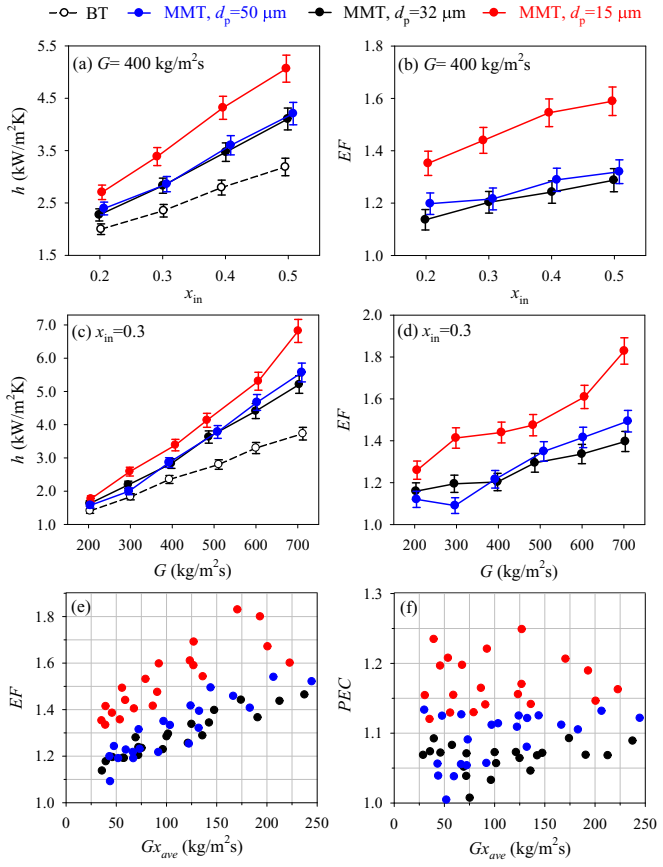

Fig. 7. The measured thermal-hydraulic characteristics of the bare tube and the three condenser tubes with MMT inserts.

transfer. The *EF* values increase by raising G and x_{in} (see Fig. 7b and d). The tube with #1 MMT insert ($d_p = 15$ μm) had the largest condensation heat transfer coefficients, reaching a maximum *EF* of 1.82. The difference between #2 and #3 MMT inserts is not obvious (see Fig. 7e). We note that heat transfer enhancement may accompany the penalty to increase pressure drop. The comprehensive performance evaluation factor *PEC* reflects the competition between the benefit of enhanced heat transfer and the penalty of increased pressure drop. A heat transfer enhancement technique can be recommended for practical application if *PEC*>1 [32]. In this paper, all the data points have *PEC*>1 to show the effectiveness of the phase separation concept for condensation improvement (see Fig. 7f).

3.2. Flow patterns in bare tube BT

Condensation heat transfer is related to flow patterns. Several important non-dimensional parameters influence flow patterns. The Froude number *Fr*, bond number *Bn* and Webber number *We* are defined as follows

$$Fr = \frac{G^2}{\rho_l^2 g D_i}, \quad Bn = \frac{(\rho_l - \rho_v) g D_i}{\sigma}, \quad We = \frac{G^2 D_i}{\rho_l \sigma} \tag{19}$$

where σ is the surface tension force and g is the gravity acceleration.

Covering the data range in this study, *Fr* is in the range of 0.411–2.295, indicating the equal importance of inertia force and gravity force. $Bn = 17444$ indicates more importance of gravity force than surface tension force. The *We* number covers the range of 107–601, meaning more importance of inertia force than surface tension force. The importance of inertia force and gravity force generates the dominant annular flow regime and stratified-wavy flow regime (see Fig. 8). The weak surface tension effect yields the narrow range of intermittent flow, which can be regarded as the transition between annular flow and stratified flow. Due to the similar reason, slug flow is not observed. The solid curves in Fig. 8 represent the measured transition boundaries, which are similar to the predictions by El Hajal et al. [37].

3.3. Annular-flow-pattern modulation with MMT inserts

The annular flow has a distinct feature to entrain droplets in vapor. This effect is enhanced for high *We* number system. These droplets impact the condenser tube wall to influence liquid film thickness. In order to study the R245fa droplet spreading on mesh-membrane surface, a high-pressure quartz-glass chamber is fabricated, including a pressurized nitrogen gas bottle, a R245fa droplet generation system, a quartz-glass chamber and an object stage (see Fig. 9). The pressurized gas creates high-pressure environment such as ~400 kPa. The droplet generation system contains a R245fa liquid reservoir, a miniature valve and a syringe needle. A single droplet, instead of droplet jet, can be generated and deposited on mesh-membrane surface. The mesh-membrane-surface is above a cavity with the margin supported by the object stage. The object stage position can be adjusted in the height direction.

Droplet spreading shows the lyophilic mesh screen surfaces to R245fa liquid (see Fig. 10a). The initial droplet diameter is 1.366 mm. The wetting morphology reflects the dynamic contact line motion governed by the interaction between droplet and mesh screen structure, showing ellipse shape on #1 twill Dutch weaved mesh screen surface, and rectangular shape on #2 and #3 plain Dutch weaved mesh screen surfaces. The #1 twill mesh screen is a 3D structure to induce ellipse spreading, but the #2 and #3 plain mesh screen is a quasi-2D structure to induce rectangular spreading. The weft wires and warp wires are crossing to form the screen structure (see Fig. 4). The different sizes of the two kinds of wires cause ellipse (not circle) spreading for #1 sample, and rectangular (not square) spreading for #2 and #3 samples. Corresponding to Fig. 10b, the capillary pressure along a mesh wire is

$$\Delta P_\sigma = 4\sigma \cos\theta \left(\frac{1}{\delta} + \frac{1}{\omega}\right) \tag{20}$$

where θ is the angle between tangent direction of vapor-liquid

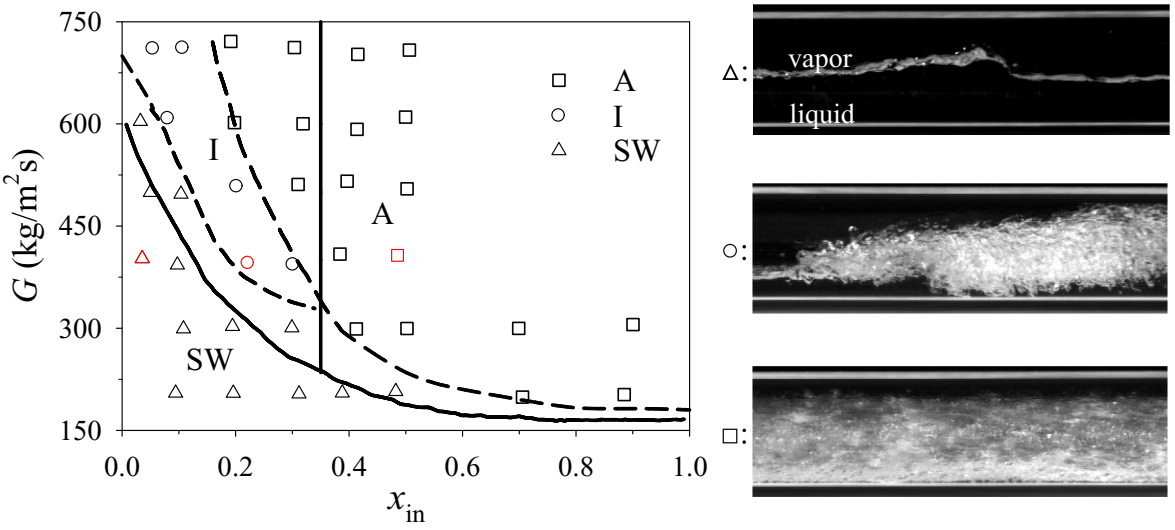

Fig. 8. Flow pattern map in bare tube (A: annular flow; I: Intermittent flow; SW: stratified-wavy flow; dotted curve: transition boundary in this paper; solid curve: transition boundary predicted by El Hajal et al. [37]).

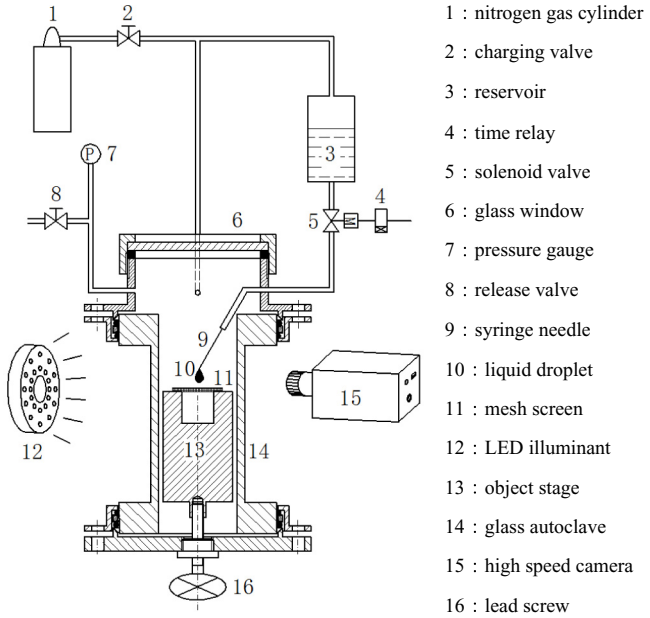

Fig. 9. The pressurized chamber for the observation of droplet dynamics of R245fa liquid.

interface and axial direction of mesh wire, ω is the vapor-liquid interface curvature, scaled by ~ d_p, δ is the mesh wire diameter, which is different for weft wire and warp wire. For example, for #1 sample, the warp wire and weft wire have $\delta_{wa} = 63\ \mu m$ and $\delta_{we} = 40\ \mu m$. For #2 sample, they are 125 μm and 63 μm for the two wires (see Table 1). The different sizes of warp wire and weft wire yield unequal capillary pressures along the two wires (see Fig. 10b). The smaller size of weft wire generates larger capillary pressure, speeding up spreading along weft wire to display ellipse shape or rectangular shape.

Fig. 10c shows the wetting area versus time, which can be correlated as

$$A_s = A_{s,max}\sqrt{1 - e^{-bt}} \tag{21}$$

where $A_{s,max}$ is the maximum spreading area, b is the attenuation coefficient, t is the time after droplet contacting with mesh screen. The smaller the b, the faster the spreading is. For #1 twill Dutch mesh screen with $d_p = 15\ \mu m$, $A_{s,max} = 46.4\ mm^2$, $b = 0.005\ s^{-1}$. For #2 plain Dutch mesh screen with $d_p = 32\ \mu m$, $A_{s,max} = 25.7\ mm^2$, $b = 0.018\ s^{-1}$. For #3 plain Dutch mesh screen with $d_p = 50\ \mu m$, $A_{s,max} = 15.9\ mm^2$, $b = 0.0256\ s^{-1}$. These results show the fastest spreading and largest spreading area on #1 mesh screen, due to the smallest pore diameter and finest mesh wires.

The mesh screen wetting is important to modulate droplet dynamics in annular gap between condenser tube wall and MMT surface (see Fig. 11). Assuming the enhanced wetting from Fig. 11a–b, the wetting area becomes larger and the liquid film thickness becomes thinner. One shall note many entrained droplets in vapor. The thinner liquid film can successfully capture latter droplets without ejecting satellite droplets after they are impacting the membrane-surface, preventing the condenser tube surface from being impacted by droplets jet (see Fig. 11b). However, thicker liquid film will be created on a not well wetted membrane surface to behave apparent contact angle. Satellite droplets jet may occur when latter droplet impact on the thicker liquid film [38]. The droplets jet will further collide with the condenser tube wall to increase the liquid film thickness, inducing heat transfer deterioration (see Fig. 11a). In summary, the #1 MMT shows the best wetting to R245fa, enhancing droplets capture capability. The condenser tube wall is less influenced by the collision of droplets, which is a new condensation heat transfer enhancement mechanism for annular-flow-pattern modulation.

3.4. Stratified-flow-pattern modulation with MMT inserts

Suspending MMT insert in tube obviously alters the stratified flow (see Fig. 12). The cross-section A-A in bare tube section far away from MMT insert is characterized by liquid height $H_{l,A}$ and vapor exposed perimeter $S_{v,A}$. The cross-section B-B with MMT insert is characterized by liquid height $H_{l,B}$ in annular gap between tube wall and MMT, and vapor exposed perimeter $S_{v,B}$. The inner diameter of sight-glass tube is $D_{gl} = 15.80$ mm, slightly larger than the copper tube diameter $D_i = 14.73$ mm. For both cross sections, S_v

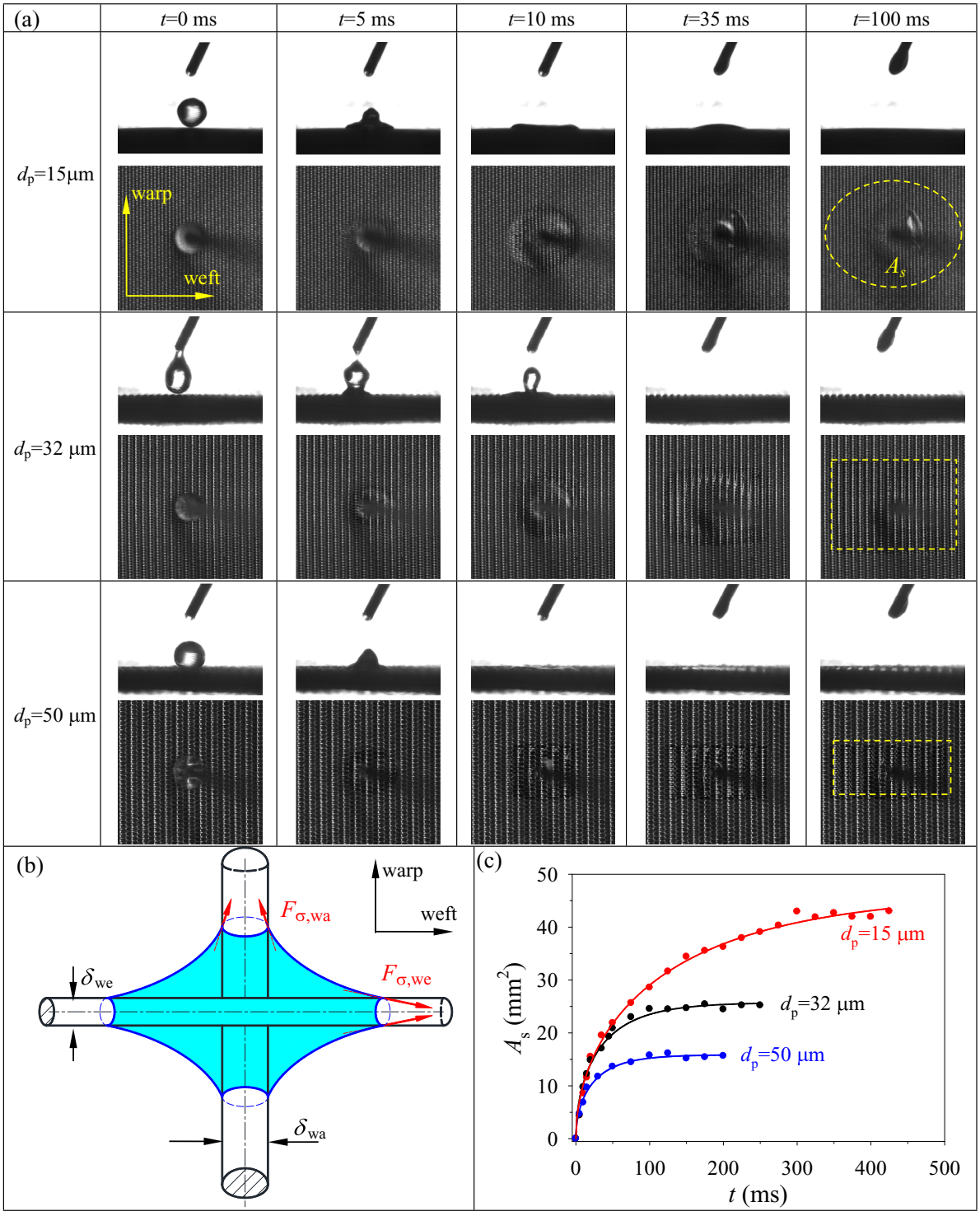

Fig. 10. Droplet spreading of R245fa liquid on mesh screen membrane.

is expressed as

$$S_v = D_{gl} \bullet \arccos\left(\frac{2H_l}{D_{gl}} - 1\right) \tag{22}$$

S_v is exposed by vapor to determine the condensation heat transfer.

When a two-phase mixture crosses from bare tube section to modulated flow section, the liquid height in annular gap is decreased. Based on our high-speed image files, the liquid height relative to inner tube diameter, H_l/D_{gl}, is plotted in Fig. 13. The data process involves a size resolution of 79 μm for liquid height. Both cross-sections A-A and B-B are given for comparison. At $G = 204.0\ kg/m^2s$ and $x = 0.104$, the bare tube section yields H_l/D_{gl} of 0.508, 0.505 and 0.510 for three independent measurements to indicate repeatable measurements of our investigation.

Different MMT induces different H_l/D_{gl} signals shown in Fig. 13.

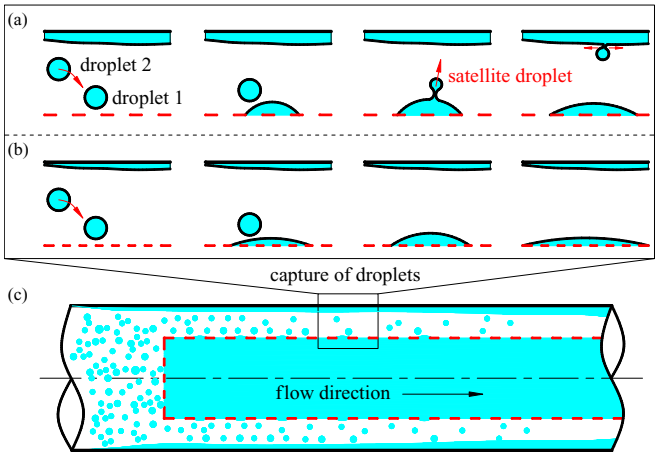

Fig. 11. Effect of droplet dynamics in annular region on liquid film thickness of the condenser tube for annular flow pattern modulation.

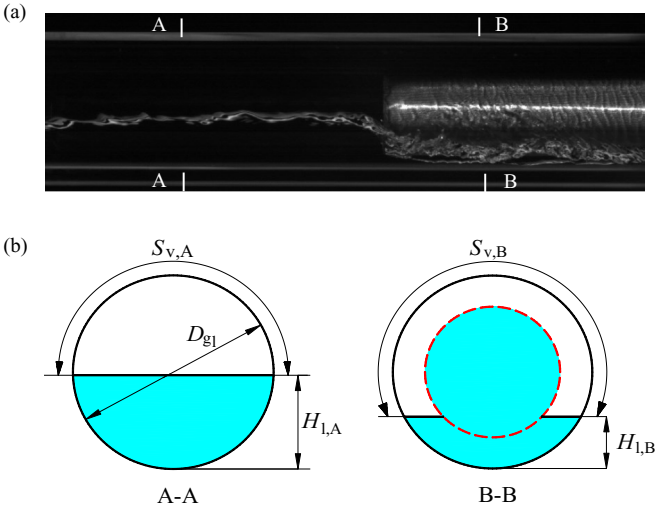

Fig. 12. The stratified-flow pattern modulation by MMT insert with $d_p = 15$ μm for $G = 204.0$ kg/m^{2}s and $x = 0.104$.

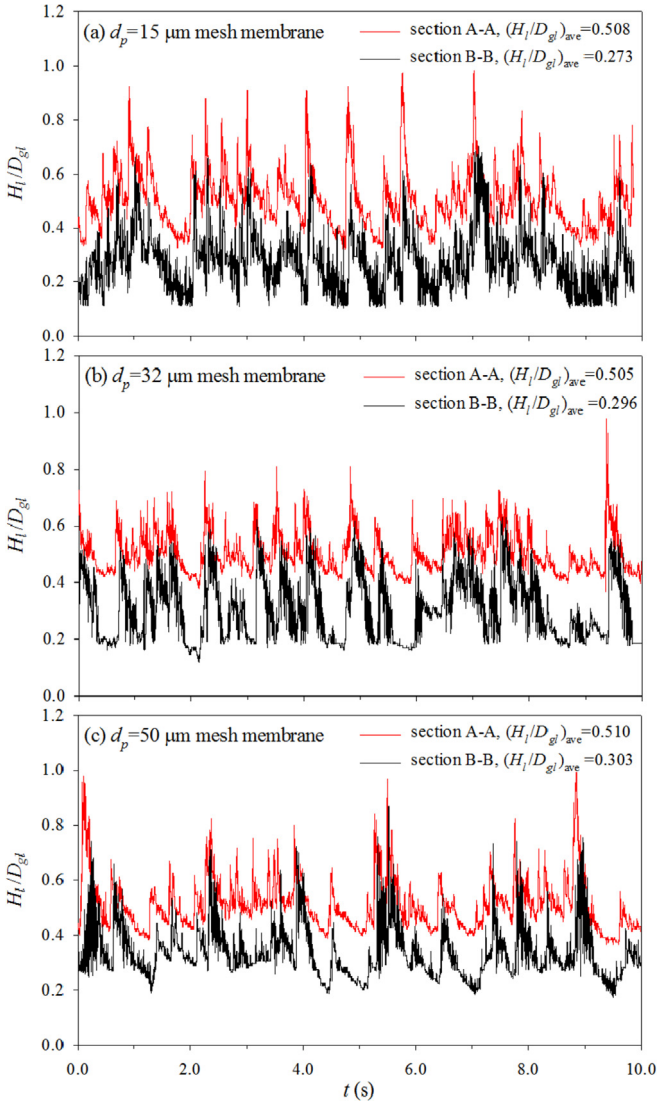

Fig. 13. Effect of different MMTs on the modulated liquid height for stratified-flow with $G = 204.0$ kg/m^{2}s and $x = 0.104$.

The time averaged values of H_l/D_{gl} are 0.273, 0.296 and 0.303 for #1, #2 and #3 MMT insert, respectively. One shall note that S_v is more sensitive to the change of H_l (see Eq. (22)). Compared with bare tube section, S_v is increased by 31.34% by #1 MMT insert, 27.57% by #2 MMT insert and 27.4% by #3 MMT insert. The smallest pore diameter of #1 MMT insert generates largest capillary force for liquid pumping from annular region to core region, explaining the best performance for #1 MMT insert.

4. Further analysis on condenser performance with MMT insert

4.1. General analysis of comprehensive condenser performance

Heat transfer coefficient can be increased by increasing vapor mass quality x and mass flux G, but large G increases pressure drop. The effects of G and x on condenser performance should be analyzed after introducing MMT insert. Condensation heat transfer in bare tube can be predicted by Eq. (15). Similarly, condensation heat transfer with MMT insert is

$$h_{MMT,pre} = 0.023\frac{\lambda_l \mathrm{Pr}_l^{0.4}}{D_i - d_o}\left[\frac{G_{an}(D_i - d_o)}{\mu_l}\right]^{0.8}\left[1 + 3.8\left(\frac{x_{an}}{1-x_{an}}\sqrt{\frac{P_{crit}}{P_{sat}}}\right)^{0.76}\right] \quad (23)$$

where d_o is the MMT insert diameter. G_{an} and x_{an} are the average mass flux and vapor mass quality in annular region, respectively. The heat transfer enhancement ratio is

$$EF = \frac{h_{MMT,pre}}{h_{BT,pre}} = K_1\left(\frac{D_i}{D_i - d_o}\right)^{0.2}\left(\frac{G_{an}}{G}\right)^{0.8} \quad (24)$$

$$K_1 = \left[\frac{1 + 3.8\left(\frac{x_{an}}{1-x_{an}}\right)^{0.76}}{1 + 3.8\left(\frac{x_{BT}}{1-x_{BT}}\right)^{0.76}}\right] \quad (25)$$

Eq. (16) is modified to calculate the frictional pressure drop with

MMT insert as

$$\Delta P_{f,MMT} = 0.3164 \frac{G_{an}^{1.5}(1-x_{an})^{1.75}\mu_l^{0.25}L_{eff}}{(D_i-d_o)^{1.25}\rho_l}\left(1+\frac{C}{X_{an}}+\frac{1}{X_{an}^2}\right) \tag{26}$$

Thus, the pressure drop penalty factor is

$$PF = \frac{\Delta P_{f,\,MMT}}{\Delta P_{f,\,BT}} = K_2\left(\frac{D_i}{D_i-d_o}\right)^{1.25}\left(\frac{G_{an}}{G}\right)^{1.5} \tag{27}$$

$$K_2 = \left(\frac{1-x_{an}}{1-x_{BT}}\right)^{1.75}\left[\frac{\frac{1}{C}+\left(\frac{x_{an}}{1-x_{an}}\right)^{0.9}+\left(\frac{x_{an}}{1-x_{an}}\right)^{1.8}}{\frac{1}{C}+\left(\frac{x_{BT}}{1-x_{BT}}\right)^{0.9}+\left(\frac{x_{BT}}{1-x_{BT}}\right)^{1.8}}\right] \tag{28}$$

In above equations, C is from 5 to 20, x_{BT} is the vapor mass quality in bare tube without insert. Based on mass conservation, we have

$$\frac{\pi}{4}D_i^2 G = \frac{\pi}{4}d_o^2 G_{co} + \frac{\pi}{4}\left(D_i^2-d_o^2\right)G_{an} \tag{29}$$

$$\frac{G_{an}}{G} = \frac{GD_i^2 - G_{co}d_o^2}{GD_i^2 - Gd_o^2} \tag{30}$$

In Eq. (29), the left side means the flow rate in bare tube, the first term and second term of right side represent the flow rates in core region and annular region, respectively. We note that G_{co} is the mass flux in core region, coming from the leakage from annular region to core region. Examining Eqs. (24), (27) and (30), one identifies that G_{co} is a key parameter to influence heat transfer enhancement and pressure drop penalty.

4.2. Extreme condition of condenser tube with solid cylinder insert

A condenser tube with solid cylinder insert is considered as an extreme case without fluid inside the cylinder body. The total flow rate either flows in bare tube, or flows in annular region ($G_{co}=0$). Identical vapor mass qualities in bare tube x_{BT} and in condenser tube with solid cylinder insert xan are assumed, yielding K_1=K_2=1 (see Eqs. (25) and (28)). Eq. (30) becomes

$$\frac{G_{an}}{G} = \frac{D_i^2}{D_i^2-d_o^2} \tag{31}$$

The heat transfer enhancement ratio is

$$EF = \left(\frac{D_i}{D_i-d_o}\right)^{0.2}\left(\frac{D_i^2}{D_i^2-d_o^2}\right)^{0.8} \tag{32}$$

The pressure drop increase penalty factor becomes

$$PF = \left(\frac{D_i}{D_i-d_o}\right)^{1.25}\left(\frac{D_i^2}{D_i^2-d_o^2}\right)^{1.5} \tag{33}$$

We note that Eqs. (32) and (33) are developed with the assumption $x_{BT}=x_{an}$. In fact, compared to bare tube, modulated heat transfer tube decreases the average vapor mass quality over a specific flow length due to the enhanced heat transfer. This effect inversely decreases the heat transfer enhancement degree. Thus, Eq. (32) represents the top-limit of heat transfer enhancement ratio. Similarly, Eq. (33) is the bottom-limit of pressure drop increase factor. In this study, $D_i=14.73$ mm and $d_o=11.40$ mm give EF<2.8 and PF>25.26. The significantly large PF leads to PEC<1, which is not acceptable for applications. However, the condenser tube with MMT insert had the measured $EF_{max}=1.82$, which can be further optimized. Most importantly, the measured PF_{max} is 8.6, which is ~1/3 of that with solid cylinder insert. The condenser tube with MMT insert not only enhances condensation heat transfer, but also decreases the pressure drop increase penalty, both coming from liquid penetration from annular region to core region.

4.3. Effect of leaking flow via membrane surface on condensation heat transfer

In this section, the similar heat transfer performance between #2 and #3 MMT inserts is analyzed. Fig. 14 shows the flow picture with axial coordinate z starting from MMT side plane. Pressures in core region and annular region at tube exit are recorded as $P_{e,co}$ and $P_{e,an}$ respectively. At a specific z, parameters are recorded as $P_{u,an}$, Gan and xan in annular region, and they are recorded as $P_{u,co}$ and G_{co} in core region. Because two-phase flow in annular region generates larger pressure drop than core region, $P_{u,an}$ is larger than $P_{u,co}$ to drive liquid flowing into core region. The mass conservation gives

$$\frac{\pi}{4}d_o^2 G_{co} = \int_0^z \pi d_o G_{leak}\,dz \tag{34}$$

where G_{leak} is the superficial mass flux across mesh-membrane-surface, noting G_{co} and G_{leak} dependent on z. By assuming mesh pores as equivalent nozzles on a solid plate, we have the following relationship between G_{leak} and driving pressure difference $P_{u,an}$-$P_{u,co}$:

$$\left(P_{u,an}-P_{u,co}\right) = K\frac{G_{leak}^2}{2\rho_l} \tag{35}$$

where K is the nozzle pressure drop coefficient [39]:

$$K = \frac{1}{C_d^2}\left(\frac{1-\varphi^2}{\varphi^2}\right) \tag{36}$$

where C_d is the nozzle discharge coefficient, which is

$$C_d = C_\infty + \frac{B}{Re_p^n} \tag{37}$$

In Eq. (37), C_∞, B and n are constants. The Reynolds number Re_p is defined as

$$Re_p = \frac{d_p G_{leak}}{\varphi\mu_l} \tag{38}$$

Substituting Eqs. (36)–(38) into Eq. (35) yields

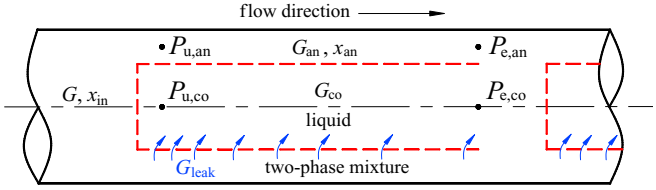

Fig. 14. The pressure balance for condenser tube with MMT insert.

$$\frac{\sqrt{1-\varphi^2}}{\varphi}\left(\frac{d_p}{\varphi}\right)^n G_{leak}^{1+n} - C_\infty\sqrt{2\rho_l(P_{u,an}-P_{u,co})}\left(\frac{d_p}{\varphi}\right)^n G_{leak}^n - B\sqrt{2\rho_l(P_{u,an}-P_{u,co})}\mu_l^n = 0 \quad (39)$$

To determine C_∞, B and n in Eq. (39), a separate experiment was performed to establish the relationship between pressure drop ΔP and flow mass flow rate m_r across mesh-membrane-surface (see Fig. 15a and b). The experiment was carried out at a R245fa temperature of 30 °C and an inlet pressure of 400 kPa. Fig. 15c indicates that all the three mesh-membrane-surfaces share a single curve of nozzle discharge coefficient C_d versus Reynolds number Re_p. The curve shown in Fig. 15c indicates the reasonable nozzle assumption. By fitting the C_d~Re_p curve, the experiment determined values are C_∞=5.95, B=−6.80 and n=0.062. Eq. (39) illustrates that G_{leak} is an implicit function of pressure difference $P_{u,an}-P_{u,co}$ and mesh pore geometry parameter d_p/φ. Even though #2 MMT (d_p=32 μm, φ=13.2%) and #3 MMT (d_p=50 μm, φ=20.0%) have different pore diameter and open porosity, d_p/φ =242.4 μm for #2 MMT is very close to d_p/φ=250.0 μm for #3 MMT, accounting for similar enhanced heat transfer performance between them.

5. Comments on the present work and comparison with other studies

In this study, the key concept for condensation heat transfer improvement is to separate two-phase mixture. The liquid leakage towards core region not only keeps well condensation heat transfer, but also achieves acceptable pressure drop penalty. Besides, mesh screen parameters influence condensation heat transfer enhancement. The smallest mesh pores of #1 MMT generate the largest capillary force for liquid pumping to keep the lowest liquid height for stratified-flow modulation. The finest mesh wires of #1 MMT insert ensures the best liquid spreading on mesh-screen-surface to prevent condenser wall from being disturbed by satellite droplets for annular flow modulation. The #1 MMT had the best performance. The similar performance of #2 and #3 MMT inserts is due to the same d_p/φ.

The capillary length is ~1 mm for most of liquids. For success phase separation, the mesh pore diameter should be one to two magnitudes smaller than the capillary length. The mesh screen has ~10 μm mesh pores. Nanofluid is useful for single-phase liquid heat transfer and boiling heat transfer. Because the long-term operation of nanofluid deposits nanoparticles on mesh wires to block mesh pores, it is not recommended when mesh screen is involved in the system. The viscous heating is another issue to be considered. When a liquid is flowing in a very small channel with ~μm diameter, the velocity gradient in radial direction is significantly large to yield viscous heating effect [40]. Because viscous heating is related to traveling distance of liquid, it is obvious only for a large flow length to diameter ratio. For present application, the mesh screen is thin in its depth direction for liquid penetrating, the viscous heating effect can be neglected.

The comparison between our present study and others is commented here. Condensation can be enhanced by three methods (see Table 4). Micro-structure on internal wall is a conventional method, which is effective for tubes having diameter smaller than ~8 mm [8–10]. This paper provides a novel phase separation mechanism, having increased EF with increase of mass fluxes and vapor mass qualities, which are different from micro-structure-based condenser tubes. The swirl flow method uses either twisted elliptical tube [41] or twisted tape insert [14]. The maximum EF is about 1.4, which is smaller the maximum EF of 1.82 reported in this study.

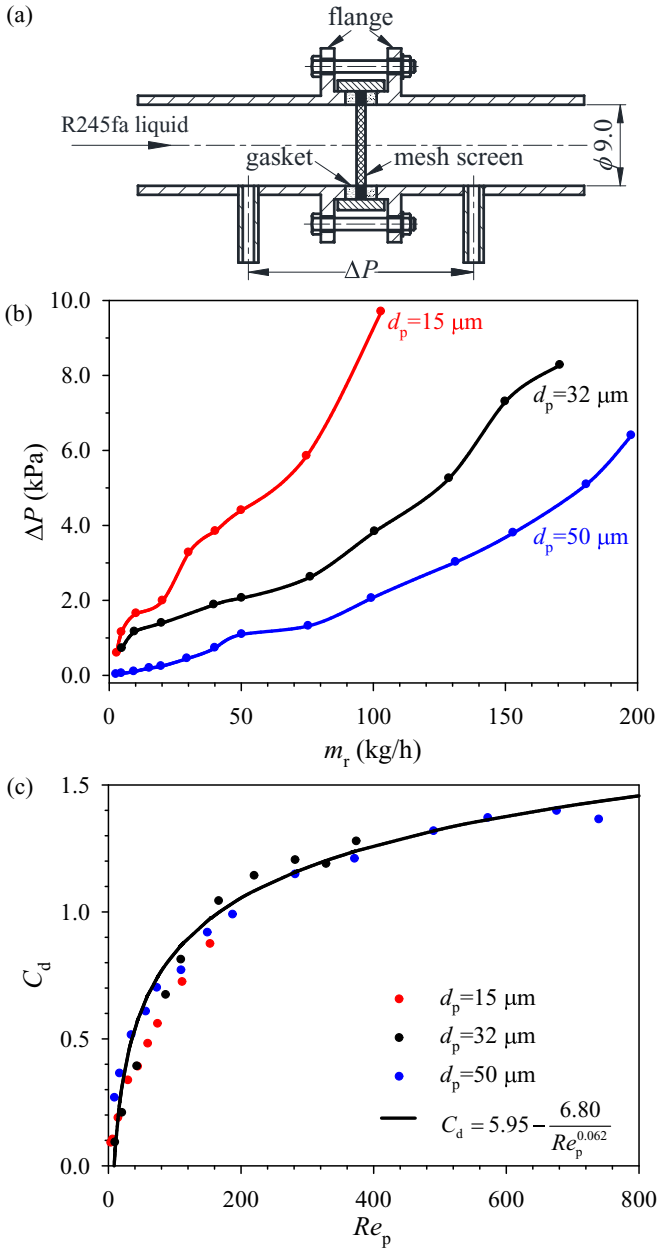

Fig. 15. The relationship between pressure drop and mass flow rate across mesh screen membrane.

In recent years, metal foam is inserted in tubes to enhance condensation heat transfer [42]. The method reaches similar heat transfer enhancement factors as our present work. The metal foam is a bulk material to cause larger material consumption, while the mesh screen membrane has light weight and is cost-effective.

The present work is useful for design and operation of condensers. First, heat transfer coefficient data obtained in this paper can be used for heat transfer design. One can decide heat transfer area and geometric parameters such as tube length and diameter. Second, it is found that heat transfer enhancement is obvious at larger Gx, inspiring us to operate condensers in suitable ranges of G and x, so that the phase separation effect is more effective. MMT inserts are recommended in the condenser upstream where x is larger than 0.1–0.2. Third, fine mesh wires and small mesh pores are recommended due to their effectiveness. Multi-layers of mesh screen pieces are suggested to enhance structure stiffness when

Table 4
The comparison between our present study and others in the literature.

References	Configuration	Working fluid and condition	Performance	Comments
Laohalertdecha & Wongwises [8]	Corrugated tube $D_i = 8.7$ mm	R134a; $T_{sat} = 40–50\,^{\circ}C$; $G = 200–700$ kg/m^{2}s; $x_{ave} = 0.1–0.9$.	$EF_{max} = 1.5$	Micro-structure on internal wall is a conventional way to enhance condensation heat transfer for small tubes.
Han & Lee [9]	Micro-fin tube $D_i = 4.00–8.92$ mm	R134a, R-22, R410A; $T_{sat} = 30\,^{\circ}C$; $G = 91–1110$ kg/m^{2}s.	$EF = 0.9–1.9$	Heat transfer enhancement degree is decreased at large mass fluxes.
Graham et al. [10]	Axially grooved tube $D_i = 8.53$ mm	R134a; $G = 75–450$ kg/m^{2}s; $x_{ave} = 0.1–0.8$.	$EF = 1.0–2.8$	Heat transfer is enhanced in a narrow parameter range.
Zhang et al. [41]	Twisted elliptical tube $D_i = 19.02$ mm	Water; $T_{sat} = 100.5\,^{\circ}C$.	$EF = 0.87–1.34$	Heat transfer enhancement is not obvious in large tubes.
Khatua et al. [14]	Twisted tape inserts $D_i = 9.4$ mm	R245fa ; $T_{sat} = 35.9\,^{\circ}C$; $G = 100–200$ kg/m^{2}s; $x_{ave} = 0.1–0.9$.	$EF_{max} = 1.375$	Limited heat transfer enhancement is obtained even using improved tube structure.
Shi et al. [42]	Metal foam insert $D_i = 22$ mm	Water, $T_{sat} = 100–139\,^{\circ}C$; $G = 100–410$ kg/m^{2}s; $x_{ave} = 0.5–0.8$.	$EF_{max} = 2.0$	A new parameter of heat transfer coefficient per unit solid structure mass is proposed.
This paper	Mesh membrane tube $D_i = 14.73$ mm	R245fa: $T_{sat} = 55.5\,^{\circ}C$; $G = 199–709$ kg/m^{2}s; $x_{int} = 0.032–0.940$.	$EF_{max} = 1.82$	The maximum heat transfer enhancement factor attains 1.82, which can be optimized in the future.

using fine mesh wires and small mesh pores.

Future works are recommended here. The phase separation using mesh screen involves fruitful bubble/droplet dynamics for two-phase mixture interacting micro-structure of mesh screen. The extended study of bubble/droplet dynamics on mesh screen enhances the understanding of phase separation mechanism. It is the time to develop a comprehensive numerical model, which can be verified by the experiment data in this paper and our previous studies [24,25]. The numerical simulation will optimize the condenser performance. Finally, the protype of phase-separation-based-condenser is expected to meet specific demand. For example, for a ~1000 MW coal fired power plant, the condenser performance becomes poor when using external air-cooling. The phase separation concept is expected to improve the condenser performance, improving the power plant efficiency.

6. Conclusions

Major conclusions found in this paper are summarized as follows.

- For condensation in bare tube, the measured heat transfer coefficients match the Shah correlation and the frictional pressured drops match the Chisholm model predictions.
- For condensation in condenser tubes with MMT inserts, the tube with #1 MMT behaves the best performance, having the heat transfer enhancement ratio of 1.82, maximally.
- For annular-flow modulation, the mesh-membrane-surface captures droplets to prevent satellite droplets from being deposited on condenser tube wall, keeping thin liquid film. This mechanism is enhanced by using smaller mesh wires such as #1 MMT.
- For stratified-flow modulation, the mesh pores generate capillary force to expose more wall area by vapor to enhance heat transfer. This mechanism is enhanced by using smaller mesh pores such as #1 MMT.
- The condenser tube with MMT insert significantly increases vapor mass qualities and maintains reasonable mass flux in annular region. Thus, the heat transfer is obviously enhanced at acceptable pressure drop increment.
- The leakage flow across membrane surface is a function of d_p/φ. Both #2 and #3 MMT inserts have similar d_p/φ, explaining similar heat transfer performances between the condenser tubes with the two inserts.
- Fine mesh wires and small mesh pores are suggested to enhance condensation heat transfer. MMT are recommended to be used in condenser tube upstream when vapor mass qualities larger than 0.1.
- Bubble/droplet dynamics interacting with mesh screen structure, numerical simulations of the complicated two-phase flow, and protype development of condensers with phase separation concept are recommended to be performed in the future.

Acknowledgements

The authors thank for the funding support by National Natural Science Foundation of China (51806065 and 51821004), China Postdoctoral Science Foundation (2017M620712) and Fundamental Research Funds for the Central Universities (2018QN031).

References

[1] Quoilin S, Orosz M, Hemond H, Lemort V. Performance and design optimization of a low-cost solar organic Rankine cycle for remote power generation. Sol Energy 2011;85:955–66.
[2] Heberle F, Brüggemann D. Exergy based fluid selection for a geothermal Organic Rankine Cycle for combined heat and power generation. Appl Therm Eng 2010;30:1326–32.
[3] Yang FB, Dong XR, Zhang HG, Wang Z, Yang K, Zhang J, Wang EH, Liu H, Zhao GY. Performance analysis of waste heat recovery with a dual loop organic Rankine cycle (ORC) system for diesel engine under various operating conditions. Energy Convers Manag 2014;80:243–55.
[4] Tchanche BF, Lambrinos G, Frangoudakis A, Papadakis G. Low-grade heat conversion into power using organic Rankine cycles–A review of various applications. Renew Sustain Energy Rev 2011;15:3963–79.
[5] Swiki AA, Joseph CD. On-site chiller testing. ASHRAE J 1990;32:54–60.
[6] Dewan A, Mahanta P, Raju KS, Kumar PS. Review of passive heat transfer augmentation techniques. P I Mech Eng A J Power 2004;218:509–27.
[7] Yu C, Xu JL, Sun YS. Transcritical pressure Organic Rankine Cycle (ORC) analysis based on the integrated-average temperature difference in evaporators. Appl Therm Eng 2015;88:2–13.

[8] Laohalertdecha S, Wongwises S. The effects of corrugation pitch on the condensation heat transfer coefficient and pressure drop of R-134a inside horizontal corrugated tube. Int J Heat Mass Tran 2010;53:2924–31.
[9] Han D, Lee KJ. Experimental study on condensation heat transfer enhancement and pressure drop penalty factors in four microfin tubes. Int J Heat Mass Tran 2005;48:3804–16.
[10] Graham D, Chato JC, Newell TA. Heat transfer and pressure drop during condensation of refrigerant 134a in an axially grooved tube. Int J Heat Mass Tran 1997;42:1935–44.
[11] Wang XW, Ho JY, Leong KC, Wong TN. Condensation heat transfer and pressure drop characteristics of R-134a in horizontal smooth tubes and enhanced tubes fabricated by selective laser melting. Int J Heat Mass Tran 2018;126:949–62.
[12] Udaya Kumar G, Venkata Krishnan D, Suresh S, Thansekhar MR, Varun Prasanna R, Jubal M. Investigating the combined effect of square microgrooves and CNT coating on condensation heat transfer. Appl Surf Sci 2019;469:50–60.
[13] Lee YR, Kuo CR, Liu CH, Fu BR, Hsieh JC, Wang CC. Dynamic response of a 50 kW organic Rankine cycle system in association with evaporators. Energies 2014;7:2436–48.
[14] Khatua AK, Kumar P, Singh HN, Kumar R. Measurement of enhanced heat transfer coefficient with perforated twisted tape inserts during condensation of R-245fa. Heat Mass Tran 2016;52:683–91.
[15] Akhavan-Behabadi MA, Kumar R, Rajabi-najar A. Augmentation of heat transfer by twisted tape inserts during condensation of R-134a inside a horizontal tube. Heat Mass Tran 2008;44:651–7.
[16] Hejazi V, Akhavan-Behabadi MA, Afshari A. Experimental investigation of twisted tape inserts performance on condensation heat transfer enhancement and pressure drop. Int Commun Heat Mass 2010;37:1376–87.
[17] Nusselt W. Die oberflachencondensation des wasserdampfes. VDI 1916;60:541–69.
[18] Breber G, Palen JW, Taborek J. Prediction of horizontal tubeside condensation of pure components using flow regime criteria. J Heat Trans T ASME 1980;102:471–6.
[19] Shah MM. A general correlation for heat transfer during film condensation inside pipes. Int J Heat Mass Tran 1979;22:547–56.
[20] Dobson MK, Chato JC. Condensation in smooth horizontal tubes. J Heat Trans T ASME 1998;120:193–213.
[21] Chen HX, Xu JL, Wang W. Internal liquid separating hood-type condensation heat exchange tube. United States Patent, US009097470B2, Aug. 4, 2015.
[22] Chen HX, Xu JL, Li ZJ, Xing F, Xie J, Wang W, Zhang W. Flow pattern modulation in a horizontal tube by the passive phase separation concept. Int J Multiphas Flow 2012;45:12–23.
[23] Chen QC, Xu JL, Sun DL, Cao Z, Xie J, Xing F. Numerical simulation of the modulated flow pattern for vertical upflows by the phase separation concept. Int J Multiphas Flow 2013;56:105–18.
[24] Xie J, Xu JL, Cheng Y, Xing F, He XT. Condensation heat transfer of R245fa in tubes with and without lyophilic porous-membrane-tube insert. Int J Heat Mass Tran 2015;88:261–75.
[25] Xie J, Xu JL, Xing F, Wang ZX, Liu H. The phase separation concept condensation heat transfer in horizontal tubes for low-grade energy utilization. Energy 2014;69:787–800.
[26] Cao S, Ji XB, Xu JL. R245fa condensation heat transfer in a phase separation condenser. Exp Therm Fluid Sci 2018;98:346–61.
[27] Yu XJ, Xu JL, Yuan JD, Zhang W. Microscale phase separation condensers with varied cross sections of each fluid phase: heat transfer enhancement and pressure drop reduction. Int J Heat Mass Tran 2018;118:439–54.
[28] Cao Z, Xu JL, Sun DL, Xie J, Xing F, Chen QC, Wang XD. Numerical simulation of modulated heat transfer tube in laminar flow regime. Int J Therm Sci 2014;75:171–83.
[29] Laohalertdecha S, Wongwises S. The effects of corrugation pitch on the condensation heat transfer coefficient and pressure drop of R-134a inside horizontal corrugated tube. Int J Heat Mass Tran 2010;53:2924–31.
[30] Smith SL. Void fractions in two-phase flow: a correlation based upon an equal velocity head model. Proc Inst Mech Eng 1969;184(1):647–64.
[31] Zhang XY, Liu ZC, Liu W. Numerical studies on heat transfer and flow characteristics for laminar flow in a tube with multiple regularly spaced twisted tapes. Int J Therm Sci 2012;58:157–67.
[32] Fan JF, Ding WK, Zhang JF, He YL, Tao WQ. A performance evaluation plot of enhanced heat transfer techniques. Int J Heat Mass Tran 2009;52:33–44.
[33] Collier JG, Thome JR. Convective boiling and condensation. third ed. Oxford: Clarendon Press; 1994.
[34] Holman JP, Gajda WJ. Experimental methods for engineers. fourth ed. Nueva York: McGraw-Hill; 1994.
[35] Xing F, Xu JL, Xie J, Liu H, Wang ZX, Ma XL. Froude number dominates condensation heat transfer of R245fa in tubes: effect of inclination angles. Int J Multiphas Flow 2015;71:98–115.
[36] Chisholm D. Pressure gradients due to friction during the flow of evaporating two-phase mixtures in smooth tubes and channels. Int J Heat Mass Tran 1973;16:347–58.
[37] El Hajal J, Thome JR, Cavallini A. Condensation in horizontal tubes. Part 1:two-phase flow pattern map. Int J Heat Mass Tran 2003;46:3349–63.
[38] Zhang FH, Li EQ, Thoroddsen ST. Satellite formation during coalescence of unequal size drops. Phys Rev Lett 2009;102:104502.
[39] Bommisetty RVN, Joshi DS, Kollati VR. Flow loss in screens: a fresh look at old correlation. J Mech Eng Autom 2013;3:29–34.
[40] Zhang LY, Xu JL, Cheng QC, Wang S. Switchable heat transfer in nano Janus-interface-system. Int J Heat Mass Tran 2018;127:761–71.
[41] Zhang L, Yang S, Xu H. Experimental study on condensation heat transfer characteristics of steam on horizontal twisted elliptical tubes. Appl Energy 2012;97:881–7.
[42] Shi J, Zheng GH, Chen ZQ. Experimental investigation on flow condensation in horizontal tubes filled with annular metal foam. Int J Heat Mass Tran 2018;116:920–30.